Microtomographic investigation of a yeast grain porous structure

F. Debaste, A. Léonard, V. Halloin, B. Haut

PII: S0260-8774(09)00579-2
DOI: 10.1016/j.jfoodeng.2009.11.012
Reference: JFOE 5936

To appear in: *Journal of Food Engineering*

Received Date: 24 July 2009
Revised Date: 6 November 2009
Accepted Date: 12 November 2009

Please cite this article as: Debaste, F., Léonard, A., Halloin, V., Haut, B., Microtomographic investigation of a yeast grain porous structure, *Journal of Food Engineering* (2009), doi: 10.1016/j.jfoodeng.2009.11.012

Microtomographic investigation of a yeast grain porous structure

F. Debaste*[,a], A. Léonard[b], V. Halloin[a], B. Haut[a]

[a] *Transfers, Interfaces and Processes, Université Libre de Bruxelles, 50, av. F.D. Roosevelt, C.P. 165/67, 1050 Bruxelles, Belgium*

[b] *Laboratory of Chemical Engineering, Department of Applied Chemistry, Université de Liege, FNRS. B6c, Sart Tilman, 4000 Liege, Belgium*

Abstract

Drying behavior of baker's yeast depends on the internal structure of the grain. In this paper, investigation of the porous structure of a dry grain using X-ray microtomography is presented. The resulting data are treated to deduce pore network characteristics for drying modeling . The treatment algorithm is based on segmentation kriging and medial axis calculation by thinning. Complementary informations are also calculated using auto-correlation function. The complete procedure is first tested on a virtual solid and then applied to yeast. The results present a large pore size distribution and a high connectivity between the pores. Both those effects can partially be attributed to the choice of the algorithms to deduce the pore network.

Key words: Yeast, microtomography, porosity, porous network

1. Introduction

Granular baker's yeast is industrially dried to reduce transport costs and to increase conservation time. This energy intensive process may cause viability loss of the product (Bayrock and Ingledew, 1997): drying conditions are crucial to achieve well inactivated yeast without causing the cells death (Volkov et al., 1990). Knowledge of the local conditions (temperature, air moisture content) inside and around the grains is therefore important to predict the yeast survival chances (Marechal et al., 1999). Thus, detailed modeling of the drying process

*Corresponding author, Tel: 00 32 2 650 67 56, Fax: 00 32 2 650 29 10
Email address: fdebaste@ulb.ac.be (F. Debaste)

would be a powerful tool to understand, control and optimize baker's yeast drying.

Most models applied to yeast drying hide the impact of the inner-grain structure on the evaporation in desorption isotherms or in fitted diffusion coefficients that have a limited physical meaning. This approach neither allows correct understanding of viability loss mechanisms nor offers a general explanation of the observed drying rate curves (Debaste et al., 2008).

Two modeling approaches have been tested recently to tackle those limitations. The first one, (Debaste et al., 2008), is based on the explicit expression of the limiting transport phenomena affecting drying considering two successive steps. This model gives satisfactory results for process optimization but no insight is gained on viability. Indeed, the assumption of a known limiting phenomenon allows hiding the impact of the porous structure in physically based fitting parameters, offering only a rough description of the inner grain phenomena.

In a second step, porous network modeling of yeast drying has been investigated (Debaste and Halloin, 2009). Although offering encouraging and well fitting results, this model was based on drastic and unrealistic assumptions about geometry and pore network topology: two dimensional slices of the grain were simulated and pore network parameters were very roughly estimated, limiting the validity scope of the results.

The global aim of this work is to obtain a more detailed, three dimensional, pore network model of the drying of yeast. This paper is focused on the investigation of the porous structure and on the deduction of a porous network to be used to model the drying.

To characterize the porosity of *Saccharomyces cerevisiae*, a living organism, the use of classical intrusive pore size identification methods, such as mercury porosimetry, gives doubtful results. Although yeast is known to survive at very high pressure (Espinasse et al., 2007), little is known about its behavior in contact with high pressure mercury. Therefore X-ray microtomographic investigation of a yeast grain is realized. This non-intrusive technique has already been

shown to be an alternative to mercury porosimetry for foam materials shrinking under the pressure (Léonard et al., 2008b). The resulting three dimensional numeric representation of the grain is then used to deduce pore network parameters.

X-ray microtomography has already been used to deduce information about the porous structure of food such as bread (Falcone et al., 2008; Babin et al., 2006), cellular foam food (Lim and Barigou, 2004; Trater et al., 2005), meat (Frisullo et al., 2009), dried bananas (Léonard et al., 2008a), apples and pears (Verboven et al., 2008). Except for the work of Verboven et al. (2008), who directly used the void space dimensions as a domain for solving numerically reaction-diffusion equations, focus was set on qualitative and simple quantitative datas. However, no complete networks parameters were deduced.

This last point has already been tested in geological science (Al-Raoush and Willson, 2005; Al-Raoush and Alshibli, 2006). In this paper, an application of similar algorithms to deduce detailed porous network in yeast grain is presented, highlighting the potential of this method for further detailed investigations.

2. Materials and methods

The applied image treatment procedure is similar to the one presented by Al-Raoush and Willson (2005). However, different algorithms are considered for the final network generation. The principle of the procedure is sketched on Figure 1. The original gray-level images (a) are segmented: every voxel is assigned to solid or void (Gonzalez and Woods, 1993). The medial axis, a one voxel thick assembly characteristic of all the paths present in the void network (Couprie et al., 2007), is then deduced (c). Finally, pore network properties are computed (d). The auto-correlation function and the tortuosity are also estimated.

This procedure, implemented in MATLAB 7.6, is tested on a computer generated set of images and then applied to experimental images obtained through X-ray microtomographic investigation of a yeast grain. The different steps are detailed in the following subsections.

2.1. Image segmentation

The simplest segmentation procedure, further called the *threshold technique*, is based on one fixed threshold: every voxel whose gray level is darker than the threshold is assigned to fluid; the rest is assigned to solid.

This method is simple but highly sensitive to background noise on the images (Oh and Lindquist, 1999). An alternative, less noise sensitive, is indicator kriging, further called the *kriging technique*, for which two thresholds are defined. Every voxel with a gray level lower than the lowest threshold is assigned to the solid and every voxel with a gray level higher than the highest threshold is put in the fluid. For intermediate values, indicator kriging, computation of the most probable value of a voxel based on the values of the surrounding voxels, is used (Oh and Lindquist, 1999). This method has two drawbacks. First, when the size of the smallest objects to be found is only of a few voxels, the treatment might suppress physically relevant informations. Second, the kriging technique requires intensive calculations. For those reasons, the two techniques are compared in our application.

2.2. Medial axis calculation

The medial axis is calculated using the thinning algorithm presented by Palagyi and Kuba (1998). The principle of this algorithm is to modify iteratively the segmented image until the only fluid voxels left form the medial axis. At every iteration, every fluid voxel neighboring a solid voxel is considered. If the configuration of the types of its neighbors fits some specifics configurations, called *masks*, the studied voxel is changed to solid. The key of this algorithm is the choice of the masks allowing to keep only the medial axis. The chosen algorithm and the corresponding set of masks are detailled by Palagyi and Kuba (1998).

2.3. Porous network identification

Different definitions of network properties are possible, depending on the goal of the network. In this paper, using the same definition as presented in Debaste and Halloin (2009), pores are defined as fluid volumes presenting no resistance to

flow. Capillary pressure, pressure drop and concentration gradient are assumed to be negligible in the pores. The pores are connected to each other by throats, that are zero volume objects where all the fluid flow resistance is concentrated : capillary pressure, pressure drop and concentration gradients in the throats are limiting the global mass transport within the network. The pores are therefore characterized by a volume and a connectivity (or pore coordination number) to a known number of throats. The throats are characterized by different parameters (global pressure drop coefficient, effective surface tension, diffusion length) to evaluate the transport phenomena limitation steps. Usually, those different parameters are correlated to the characteristic length and diameter of idealized throats (Metzger et al., 2007).

Each voxel of the medial axis which is at the intersection of multiple branches is defined as being a pore. At this stage, each pore corresponds to a single voxel. The connectivity of the different pores is evaluated by travelling on the different medial axis branches until reaching the other pores. While doing this, the distance from every voxel to the nearest solid voxel on the segmented image is calculated. The smallest value for a voxel of the medial axis between two pores is stored as being the radius of that throat.

As shown by Al-Raoush and Willson (2005), this pore definition leads to the definition of too many pores : multiple medial axis division occurs in a volume usually considered as a single pore. To solve this issue, pores are merged if the distance between them is smaller than distance between the pore and the nearest solid voxel. The new pore is located in the middle of the straight line between the two former pores. It inherits the connections of both previous pores, except the one linking the two former pores. All the pores are checked for merging one by one, iteratively, until no new merging happens.

The volume of each pore is then evaluated. Following the proposed network definition , the volume of the pore is limited by the pores walls and the connected throats. In the throat, the limit should be defined by the plan normal to the medial axis direction. However, due to the discretization of the medial axis, unsatisfactory volume division are achieved. Therefore, in this work, a simplified

evaluation is chosen, based on two iterative steps. First, all the voxels that are in the largest fully fluid sphere centered at a pore position are assigned to that pore. The pore merging step ensure that no overlapping occurs between pores. Second, every unassigned voxel neighboring an assigned voxel is assigned to the same pore. Unassigned voxels neighboring voxels assigned to different pores are assigned randomly to one of those pores. As those voxels correspond to a less than half a percent of the total number of voxels, their impact on the final volume distribution is considered to be negligible. The voxel assignment is iterated until all the fluid voxels are assigned to a pore. Counting the voxels of a pore gives its volume.

2.4. Auto-correlation function

The auto-correlation function gives the probability of having two voxels, separated by a given distance, to be both in the fluid phase. It is correlated to informations on the structure such as the specific surface, the porosity, the typical size of a constitutive element of the solid and an estimate of the length to which porosity tends to reach its macroscopic value. This last value is useful to estimate the representative elementary volume (REV) to be used in porous media modeling following the continuous approach. Indeed, the REV can be defined as the volume over which an averaged property can be considered to be independent of the position (Bear, 1972). At the length scale of the REV for porosity, the autocorrelation function must be approximately constant. The mathematical expression of the autocorrelation function was taken from Berryman and Blair (1986).

2.5. Tortuosity measurement

Tortuosity is defined to take globally into account the increased fluid path length due to the presence of the solid. It is defined the ratio between the average effective length that fluid has to follow to connect two points in the fluid phase and the Euclidian distance separating those two points.

A direct computation of porosity is obtained by travelling on the medial axis and by counting the smallest number of voxels required to go from one

pore to another. However, in this case, this is not straightforward because the uniqueness of the medial axis path between two directly connected pores is lost at the pore merging step. Therefore, in this work, it is proposed to calculate the porosity based on the product of two terms. The first one is the *throat tortuosity*, calculated for two directly connected pores before the pore merging step, and defined as the ratio between the medial axis length and the Eucledian distance between those two pores. The second one is the *network tortuosity* defined as the tortuosity between two non directly connected pores, considering that the directly connected pores are joined by straight lines.

Network tortuosity is evaluated for couples of pores distant by one third to one half of the sample dimension. For higher distances, considering a cubic sample implies that some directions present more data than others, leading to a bigger influence of those direction on a global averaged tortuosity. Inversely, for pores that are too close, the deduced porosity represent a too local value.

2.6. Virtual solid for validation

To validate the method, the complete algorithm is tested on a virtual sample of known properties. The fluid phase is defined by the junction of regular octahedrons of uniformly distributed size but centered on a regular cubic lattice. The minimal and maximal value of the size distribution is chosen to ensure that every octahedron is in contact with its six neighbors. Figure 2 presents the visualisation of the void structure for 2x2x2 octahedrons already voxelized (presented as small cubes). Figure 3 illustrates a slice in a structure of 10x10x10 octahedrons (white is void, black is solid).

For this solid, the throats have a square section with a side length d_{lia} given by

$$d_{lia} = \left(\frac{\sqrt{2}}{2} \overline{d_o} \right) - L_o, \tag{1}$$

where $\overline{d_o}$ is the average of the length of the border of the two connected octahedrons and L_o is the distance between the center of two successive octahedron.

Similarly, the volume of a pore, obtained by truncating the full octahedron, writes as

$$V_{pore} = \left(\frac{\sqrt{2}}{3} d_o^3\right) - \frac{\sqrt{2}}{6} \sum_{lia} d_{lia}^3. \quad (2)$$

Exact throat tortuosity is 1 and the averaged isotropic network tortuosity is of 1.52. The generated samples contain 1000 pores with normally randomized sizes and distributed in 100x100x100 voxels. For a comparison with the experimental images obtained by microtomography, the voxel length is chosen to be 2.95 μm, which is the calibrated voxel size for the yeast samples.

2.7. Noise addition to the virtual solid images

To test noise influence, present on experimental samples, a perturbed volume is computed based on the previously defined void space. A gray level in a range of 64 values , based on a normal random distribution, is given to every voxel. A different distribution is applied for fluid and for solid voxels. Both distributions have the same standard deviation but different averages. The solid distribution center is set on the 22nd gray level while the fluid is centered on the 43rd. Different noise standard deviation are tested going from 2.5 to 7.5 gray levels.

2.8. Microtomographic imaging of yeast grains

The analyzed *Saccharomices Cerevisiae* grains are industrially produced by Beldem (Andenne, Belgium) and then dried in a desiccator during one week at 25°C and 5 % of relative humidity. The microtomographic investigation was realized using a *Skyscan-1172 high-resolution desktop micro-CT system* (Skyscan, Kontich, Belgium). A dried yeast sample was placed vertically in a polystyrene holder, the latter being almost transparent to X-rays. The cone beam source operated at 60 kV and 167 μA. The detector is 2D, 1048x2000 voxels, 16-bit X-ray camera. The distance source-object-camera was adjusted to produce images with a voxel size of 2.95 μm. The rotation step was fixed at 0.4°. For each angular position, a radiograph of the sample, was recorded by a 2D camera. The Feldcamp back projection algorithm was used to reconstruct 2D images of the cross-sections of the sample from the radiographs. The corresponding yeast

3D image is obtained by stacking the 2D cross-sections. The obtained 3D image is 1024x1024x1024 voxels wide.

3. Results

3.1. Application of the algorithm to the virtual solid

Ten solids, with no noise addition, were generated and tested with the full algorithm. No significant differences were observed between those ten solids.

The network deduction of the virtual solid leads to 1070 pores in average, instead of 1000. Figure 4 presents the coordination number of the different pores. Globally, predictions are satisfactory although toward lower values, a bias is observed. The merging algorithm leads to two error types that can explain the discrepancies. First, two pores that should be merged are not, leading to pores with lower coordination. Second, two pores that should not be merged are, leading to a highly coordinate pore.

As the total pore number is higher than theoretically, for this sample, the first error is slightly more present. Enhancing the resolution (number of voxel per pore) would lower both errors. For the virtual solid, only the computational power limits the resolution. For the yeast sample, measurement resolution is the limiting factor.

Figure 5 presents the throat size distribution. As the throat size is the smallest element to be identified, it is more affected by resolution limitation than other parameters. For the chosen resolution, only four different sizes can be distinguished. Indeed, the largest possible throat radius is only 8 time the estimated error on the radius measurement which is of around 2 voxels. The obtained size is globally underestimated. Tests with a higher resolution confirm the ability of the algorithm to reduce this error.

Figure 6 shows the pore volume distribution. Theoretically, as obtained from equation (2), the pore size should be, in the studied case, divided in four well marked peaks. However, although two of those peaks are predicted, these are included in a bell-shaped curve. The average value of the distribution is however

well predicted. The simplified algorithm proposed in this work is thus unable to predict multimodal porosity.

The predicted throat tortuosity is 1.045, which is only slightly overevaluated. The network tortuosity is estimated at 1.41, which corresponds to a 10 % underestimation.

3.2. Impact of the segmentation algorithm

The virtual solid volume with different noises is submitted to the two segmentation algorithms with various segmentation thresholds. Figure 7 presents the percentage of wrongly attributed voxels for various threshold values with different noises. For the kriging, where two thresholds have to be set, the abscissa value corresponds to the lower threshold value. The higher threshold is fixed seven grey levels higher. As expected, the number of errors are minimal for both methods exactly at the average of the mean of the distributions. Except when the noise is really small, the kriging leads to less errors than the one level technique. However, kriging only leads to maximum 25% less errors than the other method.

Bloc	1		2		3	
Method	Kriging	Thres.	Kriging	Thres.	Kriging	Thres.
Simple threshold		72		78		76
Lowest kriging threshold	71		75		73	
Highest kriging threshold	75		79		77	
Porosity	0.581	0.581	0.5805	0.579	0.5975	0.597
Specific surface (m^{-1})	123000	123000	115600	115600	114100	114100
Mean coordination number	4.63	4.46	4.41	4.32	4.72	4.55
Median coordination number	4	4	4	4	4	4
Pores number	1536	1678	1582	1676	1518	1658
Throats number	7104	7496	6981	7242	7168	7545
Average pore volume (μm^3)	9200	8500	9400	8900	10100	9300
Throat tortuosity	1.33	1.31	1.30	1.30	1.37	1.36
Network tortuosity	1.53	1.53	1.55	1.54	1.61	1.58

Table 1: Comparison of yeast analysis results for 3 different samples.

3.3. Application to yeast

Figure 8 illustrates a reconstructed 2D slice obtained by X-ray microtomography for a dry yeast grain.

Segmentation parameters and results for three regions of 100x100x100 voxels inside the yeast grain are summarized in Table 1. The segmentation threshold is unknown, it is chosen to achieve a global porosity around 0.6 which was estimated experimentally using a gravimetric method. Table 1 shows a fairly good reproductivity of the results. Details are therefore given only for one sample.

Figure 9 presents the coordination number of pores for the two segmentation techniques. Both methods show similar results. A very large range of value is observed. Such distributions have been reported previously with similar algorithm applied to porous rocks (Baldwin et al., 1996; Al-Kharusi and Blunt, 2006). The large values of coordination numbers can be attributed to the definition given to a pore. Indeed, as every crossing of the medial axis is initially considered as a pore, every irregularity in the solid structure leads to the definition of a pore. The pore merging step reduces that effect, but leads to highly connected pores. Globally, pores with a coordination number superior to 8 represents less than 10% of the total and therefore only play a minor role. Pores having a coordination number of 2 are also present. These pores appears at the crossing of medial axis branches leading outside the sample. Such pores do not affect the connectivity of the network and are therefore generally suppressed. Their volume is added to the pore connected with the largest throat. The smaller throat is assigned to link the two pores connected to the suppressed one.

The throat diameter distribution is presented on Figure 10. No major difference can be stressed out between the two segmentation techniques. Most observed throats have a diameter of maximum 3 voxels, which is estimated just above the error of the throat size evaluation. The largest throats are only 3 times larger. Therefore, few informations can be deduced as the measurement resolution is limiting.

Similarly, the pore volume distribution is presented on Figure 11. As for the throats, a non negligible fraction of the pores have a size corresponding to the estimated precision of our algorithm. However, a very large size distribution

can be observed. As shown for the virtual solid, this distribution has to be interpreted with care as the methodology does not allow to predict multimodal porosity.

Also, the auto-correlation function predicts a porosity REV typical length scale of about 100 μm.

4. Analysis and discussion

The analysis of a limited region of 100x100x100 voxels allows the computation of a set of average values characterizing the network of a yeast grain. The validity of using a reduced part of the grain is supported by both the reproductivity of the results for different regions of the grain and the fact that the autocorrelation function predicts a REV typical length three times smaller than the considered region. This value ensures that for common applications, where a grain is of a millimetric size, the continuous modeling approach can be used to describe the global behavior of the grain.

The choice of the segmentation technique seems to have only a limited impact on the deduced network and other averaged properties. Three main reasons can explain this :

1. the rest of the image treatment is not affected by the observed variations in segmentation,
2. the thresholds used were correctly estimated,
3. the noise on the samples is too high for the difference between the methods to be significant.

The average coordination number obtained is of the order of 4, which corresponds to the coordination number of the void space of a monodisperse dense sphere packing. This value is therefore acceptable. A few pores have an unrealistically high coordination number, due to their deduction from a highly noise sensitive medial axis.

The throat size distribution is barely exploitable due to limitation in the resolution method. However, more careful treatment algorithm (based on the

whole throat section measurement rather than on their radius) could already offer better results using the same images. The obtained results only allows a rough description of the throats. This information is however the first to be available.

For the pore volume size distribution, also, a gross estimate has been obtained. Alternative algorithm for this step should be considered.

The results can be used as input parameters for different models. Except for the pore volume distribution, for which the results are not reliable, all the other parameter measurement present a net enhancement compared to the data previously used in Debaste and Halloin (2009).

The tortuosity and the approximate size of the REV are useful information to be used in continuous models, such as the one presented in Debaste et al. (2008). The total tortuosity obtained by this analysis is around 2, which is of an acceptable order of magnitude. However this value is lower than the value used in Debaste et al. (2008), where tortuosity, used as a fitting parameter, was evaluated around the value of 5, suggesting a need for further model refinement.

5. Conclusion

A general simplified method to deduce porous structure, based on existing algorithms, was presented, tested and applied to 3D images of granular yeast obtained by X-ray microtomography. This algorithm allows detailed investigation of the porous structure without altering the structure of the material, offering valuable information for inner grain drying modeling.

Pore and throat size distributions, connectivity, specific surface, tortuosity and REV size have all been determined. However, both algorithm approximations and experimental resolution limitations limit the scope of the results. The obtained results can however be directly integrated in existing models for which simpler assumptions had been previously taken. Enhancement of the presented algorithm could lead to more precise data, fully satisfactory for all the considered modeling approaches.

Acknowledgements

F. Debaste and A. Léonard acknowledge financial support from the Fonds National de la Recherche Scientifique (FRS-FNRS), Belgium

References

Al-Kharusi, A. S., Blunt, M. J., 2006. Network extraction from sandstone and carbonate pore space images. Journal of petroleum science and engineering 56 (4), 219–231.

Al-Raoush, R., Alshibli, K., 2006. Distribution of local void ratio in porous media systems from 3D X-ray microtomography images. Physica A 359, 713–728.

Al-Raoush, R., Willson, C., 2005. Extraction of physical realistic pore network properties from three-dimensional synchrotron X-ray microtomography images of unconsolidated porous media systems. Journal of hydrology 300, 44–64.

Babin, P., Valle, G. D., Chiron, H., Cloetens, P., Hoszowska, J., Pernot, P., Rguerre, A., Salvo, L., Dendievel, R., 2006. Fast x-ray tomography analysis of bubble growth and foam setting during breadmaking. Journal of Cereal Science 43 (3), 393 – 397.

Baldwin, C., Sederman, A. J., Mantle, M., Alexander, P., Gladden, L., 1996. Determination and characterization of the structure of a pore space from 3D volume images. Journal of colloid and interface science 181, 79–92.

Bayrock, D., Ingledew, W., 1997. Fluidized bed drying of baker's yeast : moisture levels, drying rate, and viability changes during drying. Food research international 30 (6), 407–415.

Bear, J., 1972. Dynamics of Fluids in porous media. Dover Publication, Haifa.

Berryman, J., Blair, S., Sep. 1986. Use of digital image analysis to estimate fluid permeability of porous materials: application of two-point correlation function. Journal of Applied Physics 60 (6), 1930–1938.

Couprie, M., Coeurjolly, D., Zrour, R., 2007. Discrete bisector function and euclidean skeleton in 2D and 3D. Image and vision computing 25 (10), 1543–1556.

Debaste, F., Halloin, V., 2009. Application of discrete modelling approach to fluidized bed yeast drying. Journal of food process engineeringUnder press.

Debaste, F., Halloin, V., Bossart, L., Haut, B., 2008. A new modeling approach for the prediction of yeast drying rates in fluidized beds. Journal of food engineering 84, 335–347.

Espinasse, V., Perrier-Cornet, J.-M., Marecat, A., Gervais, P., Jun. 2007. High pressure inactivation of dried microorganisms. Biotechnology and bioengineering.

Falcone, P. M., Daiano, A., Zanini, F., Mancini, L., Tromba, G., Montanari, F., Del Nobile, M. A., 2008. A novel approach to the study of bread porous structure: Phase-contrast x-ray microtomography. Journal of food science 69 (1), FEP38 – FEP43.

Frisullo, P., Laverse, J., Marino, R., Del Nobile, M., 2009. X-ray computed tomography to study processed meat microstructure. Journal of Food Engineering In Press, Corrected Proof, –.

Gonzalez, R., Woods, R., 1993. Digital image Processing. Addison Wesley Longman.

Léonard, A., Blacher, S., Devahastin, S., 2008a. Effect of far-infrared radiation assisted drying on microstructure of banana slices: An illustrative use of x-ray microtomography in microstructural evaluation of a food product. Journal of Food Engineering 85, 154–162.

Léonard, A., Calberg, C., Kerckhofs, G., Wevers, M., Jérôme, R., Pirard, J.-P., Germain, A., Blacher, S., 2008b. Characterization of the porous structure of biodegradable scaffolds obtained with supercritical CO2 as foaming agent. Journal of porous materials 15, 397–403.

Lim, K., Barigou, M., 2004. X-ray micro-computed tomography of cellular food products. Food Research International 37 (10), 1001 – 1012.

Marechal, P., Martinez de Marnanon, I., Poirier, I., Gervais, P., 1999. The importance of the kinetics of application of physical stresses on the viability of microorganisms: significance for minimal food processing. Trends in food science and technology 10, 15–20.

Metzger, T., Tsotsas, E., Prat, M., 2007. Modern Drying Technology. Vol. 1. Wiley-VCH Verlag, Ch. 2. Pore network models : a powerful tool to study drying at the pore level and understand the influence of structure on drying kinetics, pp. 49–57.

Oh, W., Lindquist, W., Jul. 1999. Image thresholding by indicator kriging. IEEE transaction on pattern analysis and machine intelligence 21 (7), 590–602.

Palagyi, K., Kuba, A., 1998. A 3D 6-subiteration thinning algorithm for extracting medial lines. Pattern recognition 19, 613–627.

Trater, A., Alavi, S., Rizvi, S., 2005. Use of non-invasive x-ray microtomography for characterizing microstructure of extruded biopolymer foams. Food Research International 38 (6), 709 – 719.

Verboven, P., Kerckhofs, G., Mebatsion, H., Tri Ho, Q., Temst, K., Wevers, M., Cloetens, P., B.M., N., 2008. Three-dimensional gas exchange pathways in pome fruit characterized by synchrotron x-ray computed tomography. Plant physiology 147 (2), 518.

Volkov, V., Sakharov, B., Shchepkin, V., Fedyukina, G., Kashuba, A., Mar. 1990. On the nature of yeast cells resistance to drying. Mikrobiologiya 61 (2), 214–222.

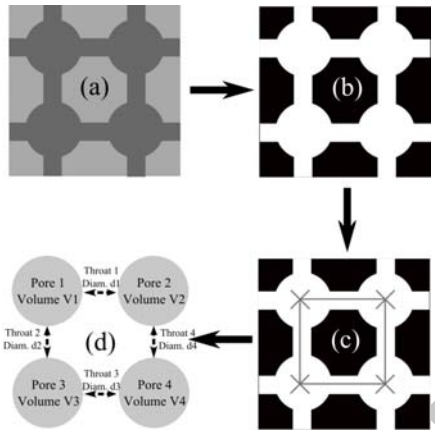

Figure 1: Different steps of image treatment to extract the network information.

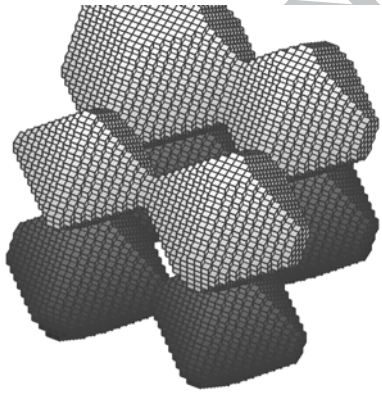

Figure 2: Virtual solid visualisation.

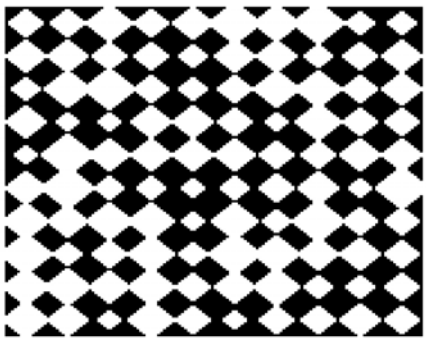

Figure 3: Virtual solid slice visualisation (void is in white, solid is in black).

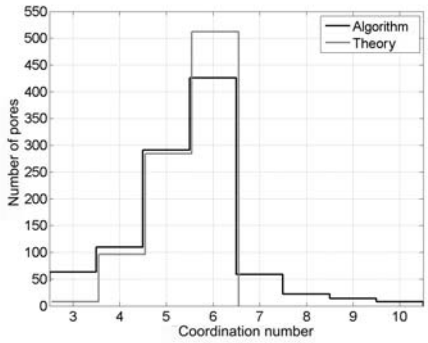

Figure 4: Predicted and theoretical coordination number of the virtual solid.

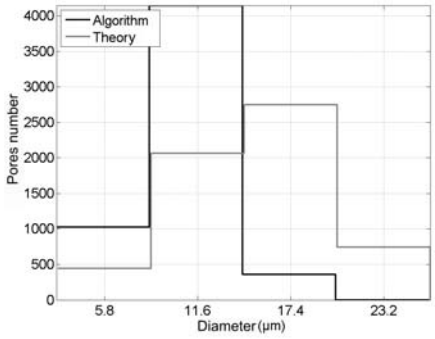

Figure 5: Predicted and theoretical throat diameter of the virtual solid.

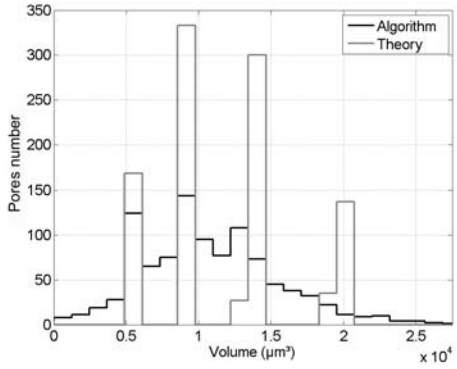

Figure 6: Predicted and theoretical pore volume distribution of the virtual solid.

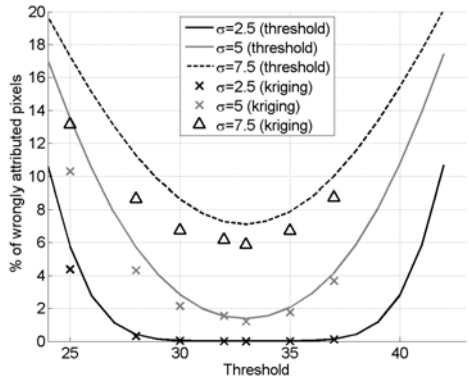

Figure 7: Fraction of wrongly attributed voxels using different segmentation techniques.

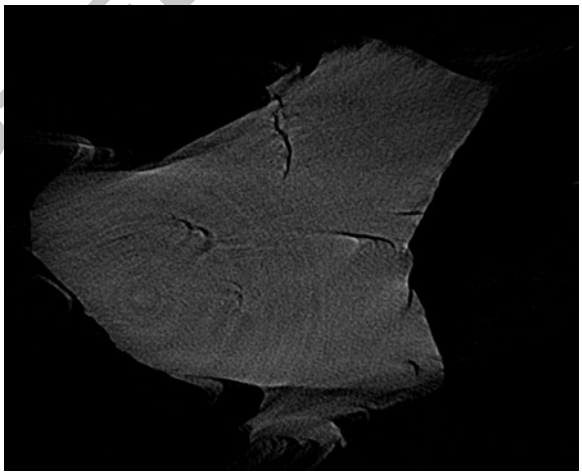

Figure 8: A reconstructed 2D yeast grain slice, obtained by microtomography.

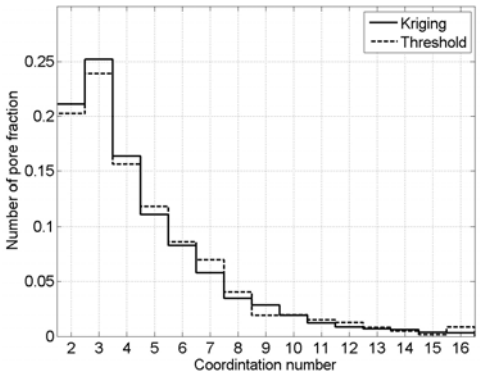

Figure 9: Coordination number for a yeast sample.

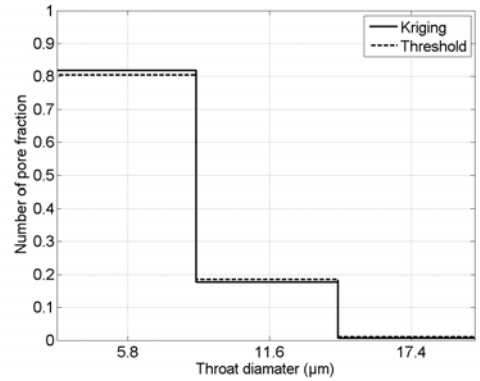

Figure 10: Throats diameters distribution for a yeast sample.

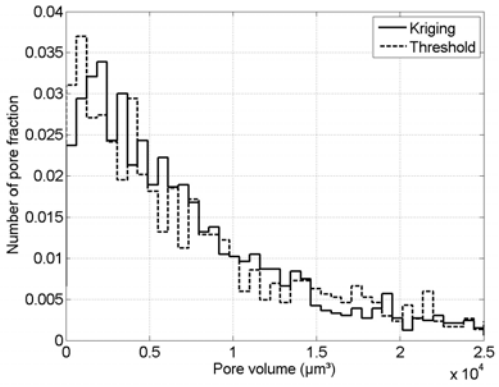

Figure 11: Pores volume distribution for a yeast sample.